International Communications in Heat and Mass Transfer 169 (2025) 109639

Contents lists available at ScienceDirect

International Communications in Heat and Mass Transfer

journal homepage: www.elsevier.com/locate/ichmt

Topology optimization of microchannels for a solid-state lithium target based on entransy dissipation theory

Zhao Xijun [a,b], Qin Kaiwen [a,b], Lv Tingxiang [a,b], Yang Si [a,b], Zheng Wei [c], Li Jun [d], Tang Xiaobin [a,b,*]

[a] Department of Nuclear Science and Technology, Nanjing University of Aeronautics and Astronautics, Nanjing 211106, China
[b] Key Laboratory of Advanced Nuclear Technology and Radiation Protection, Ministry of Industry and Information Technology, Nanjing 211106, China
[c] Beijing Institute of Astronautical Systems Engineering, Beijing 100076, China
[d] School of Chemistry and Chemical Engineering, Harbin Institute of Technology, Harbin 150001, China

ARTICLE INFO

Keywords:
Topology optimization
Microchannel
Entransy dissipation rate
Boron neutron capture therapy
Multi-objective

ABSTRACT

Boron neutron-capture therapy (BNCT) employs accelerator-driven solid-state lithium targets to generate neutrons. The targets experience a high thermal load due to proton bombardment, with a heat flux exceeding 300 W/cm^2. The low-melting-point of lithium (179 °C) brings more challenges in thermal design. Conventional microchannel cooling has two drawbacks: non-uniform temperature distribution and flow dead zone. Most of the previous topology optimization (TO) strategies focused on average temperature field and fluid dissipation power. However, they seldom considered temperature field uniformity. To solve this limitation, the present study proposes a novel triple-objective TO framework. This approach incorporates the entransy dissipation rate alongside average temperature and fluid dissipation power. The combined objectives aim to enhance hotspot suppression, reduce flow resistance, and improve global heat transfer performance. A density-based TO method was implemented in COMSOL Multiphysics using the method of moving asymptotes for a 2D axisymmetric model. There were four optimized models: M1 (dual-objective, single-inlet/single-outlet), M2 (triple-objective, single-inlet/single-outlet), M3 (dual-objective, dual-inlet/dual-outlet), and M4 (triple-objective, dual-inlet/dual-outlet). The most important point is that M4 got the best synergy: Compared with M1, the peak temperature decreased by 20 % and it was 407.79 K. Compared with M3, the pressure drop was reduced by 24.2 % and it was 46.7 kPa. Compared with M3, the performance evaluation criterion was increased by 67.5 % and it was 1.678. The multiple objectives can resolve the conflict between them. This provides an innovative design paradigm for high heat flux in heat sink for BNCT targets.

1. Introduction

Boron neutron-capture therapy (BNCT) enables targeted tumor destruction through high-LET particles released from the $^{10}B(n,\alpha)^7Li$ nuclear reaction [1]. Accelerator-driven neutron sources have emerged as the mainstream approach owing to their safety and controllable neutron yields [2,3]. Among these, solid-state lithium targets have attracted attention because of their low proton energy (2.5 MeV) and high neutron yield [4–6]. However, solid-state lithium targets encounter significant thermal management challenges due to the low melting point (179 °C) and high chemical reactivity of lithium metal, which increase susceptibility to temperature-induced failure. The localized ultrahigh heat flux (>300 W/cm^2) generated by proton-beam bombardment imposes extreme demands on cooling systems. The existing thermal management strategies include the following:

(1) Target structure innovations (e.g., a rotating target achieving 78 °C temperature control [7]; a three-rotating-port target meeting 2.5 MeV/20 mA cooling requirements [8,9], alongside stationary systems such as conical lithium targets [10–13],as shown in Fig. 1);

(2) Active cooling enhancements (e.g., 13 3.7 mm-spaced rectangular channels enabling stable 10-cm Li target operation at 10 mA proton beam with 10 m/s flow [14]). However, fundamental limitations persist: passive cooling designs approach physical efficiency limits, whereas active microchannel cooling is constrained by manufacturing complexity. Neither effectively addresses temperature nonuniformity

* Corresponding author at: Room B224, Key Laboratory of Advanced Nuclear Technology and Radiation Protection, Ministry of Industry and Information Technology, Nanjing 211106, China.
E-mail address: tangxiaobin@nuaa.edu.cn (T. Xiaobin).

https://doi.org/10.1016/j.icheatmasstransfer.2025.109639

Available online 9 September 2025

Nomenclature

BNCT	Boron Neutron Capture Therapy
C_p	Specific heat capacity(J/(kg·K))
D_h	Hydraulic diameter(m)
Da	Darcy Number
EDR	Entransy dissipation rate(W·K)
F	Average Temperature Factor
H	Overall height(mm)
H_{ch}	Flow channel height(mm)
J	Total objective function
k	Thermal conductivity(W/(m·K))
L	Overall length(mm)
high-LET	High linear energy transfer
Nu	Nusselt number
PEC	Performance evaluation criterion
ΔP	Pressure drop (Pa)
q	Heat flux(W/m^2)
R	Filter radius
Re	Reynolds number
SST	Shear stress transport
S	Area(m^2)
TO	Topology optimization
T_w	Average heated-surface temperature(K)
T_f	Average fluid bulk temperature(K)
T_{max}	Maximum heated-surface temperature(K)
T_{avg}	Average heated-surface temperature(K)
u	Velocity (m/s)
W	Overall width(mm)
W_{ch}	Flow channel inlet width(mm)
γ	Continuous design variable
$\alpha(\bar{\gamma})$	Damping coefficient
ω_T	Weighting coefficients for temperature
ω_f	Weighting coefficients for flow resistance
ω_h	Weighting coefficients for entransy dissipation rate
ρ	Density(kg/m^3)
μ	Dynamic viscosity(Pa·s)
β	Projection slope parameter
η	Projection threshold
∇T	Temperature gradient(K/W)

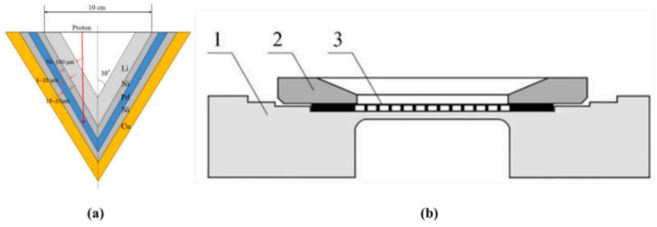

Fig. 1. Schematic illustration of (a) V-shaped target structure; (b) rectangular cooling channel (used in conventional lithium target cooling, exhibiting flow dead zones).

[15].

Topology optimization (TO) enables breakthroughs in microchannel design through autonomous topology generation. Enhanced thermal performance has been demonstrated in forced-convection heat sinks [16–18], natural convection systems [19,20], and bioinspired configurations [21,22]. The pursuit of optimal designs in thermo-fluid systems often involves balancing conflicting objectives, such as minimizing temperature and flow resistance [23,24]. This has led to the widespread adoption of multi-objective optimization (MOO) algorithms. Recent years have witnessed significant advancements in MOO algorithms, greatly enhancing our capability to explore complex design spaces. Algorithms such as the Multi-objective Geometric Mean Optimizer (MOGMO) [25], Multi-objective Exponential Distribution Optimizer (MOEDO) [26], and Multi-objective RIME Algorithm (MORIME) [27] have demonstrated robust performance in terms of convergence and diversity of solutions. Furthermore, novel approaches like the Elitist Non-dominated Sorting Harris Hawks Optimization [28], Multi-objective Gradient-Based Optimizer [29], and Multi-Objective Slime Mould Algorithm [30] have enriched the toolbox available to researchers. Despite these powerful computational advancements, their application specifically to the topological design of microchannels for managing ultra-high heat flux in targets like those for BNCT remains limited. However, microchannel optimization inherently requires a balanced temperature and flow resistance minimization.

To overcome the limitations of conventional dual-objective strategies, we propose a novel triple-objective TO framework. Building on the minimization of the average temperature factor(F)and fluid dissipation power(W_f), the entransy dissipation rate(EDR)was introduced as the third objective [31]. The EDR quantitatively captures the irreversible loss of heat transfer potential, and its minimization directly promotes reduced temperature gradients and improved uniformity. This approach allows us to simultaneously address local hotspot suppression, global heat transfer efficiency, and flow resistance control. Furthermore, we explore the synergy between this advanced optimization goal and innovative dual-inlet/outlet configurations. This integrated methodology provides a new design paradigm for high-heat-flux thermal management in BNCT applications and beyond.

2. Triple-objective topology optimization theoretical framework

2.1. Model construction and boundary conditions

The study adopted a density-based TO framework using the method of moving asymptotes (MMA). Material distribution was described by a continuous design variable fieldγ, whereγ = 1represents solid copper andγ = 0represents fluid water. This study used COMSOL Multiphysics 6.2 to optimization design. A two-dimensional axisymmetric model (Fig. 2) was established with a radius of 120 mm and an axial height of 60 mm. A circular heat source region of 50 mm radius was subjected to a uniform heat flux of 300 W/cm^2, corresponding to a total power of 23,550 W. Boundary conditions were established to simulate practical cooling systems: a constant pressure inlet (10 Pa) was applied on the 10 mm wide inlet section, a zero-pressure outlet (0 Pa) was set, and all other walls were set as adiabatic no-slip surfaces. The global fluid volume fraction was constrained to ≤50 %. The properties of the materials used

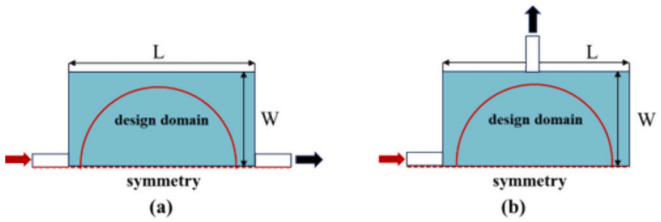

Fig. 2. (a) Two-dimensional topology optimization model with single entry and single exit; (b) Two-dimensional topology optimization model with two entries and two exits.

in the simulation are listed in Table 1.

(b) Two-dimensional topology optimization model with two entries and two exits.

2.2. Governing equations and material interpolation

Helmholtz density filtering smoothing was applied for the elimination of numerical instabilities caused by discontinuous jumps of the design variables.

$$-R^2\nabla^2\widetilde{\gamma}+\widetilde{\gamma}=\gamma \tag{1}$$

Filter radius (R) was 1.5 times the mesh size. Interface sharpening was achieved using the Heaviside projection Eq. [32]:

$$\widehat{\gamma}=\frac{\tanh(\beta(\widetilde{\gamma}-\eta))+\tanh(\beta\eta)}{\tanh(\beta(1-\eta))+\tanh(\beta\eta)} \tag{2}$$

$\beta$is the projection slope parameter and η is the projection threshold.

Fluid flow was governed using the Brinkman penalization model [33]:

$$\rho(u\cdot\nabla)u=-\nabla p+\nabla\cdot(\mu\nabla u)-\alpha(\widetilde{\gamma})u \tag{3}$$

The damping coefficient $\alpha(\widetilde{\gamma})$ was defined by the Darcy interpolation model:

$$\alpha(\widetilde{\gamma})=\alpha_{\max}\frac{(1-\widetilde{\gamma})q}{q+\widetilde{\gamma}}(q=0.05) \tag{4}$$

Following the established research [34], $\alpha_{\max}$was set to 10°to ensure sufficiently low velocities in the solid regions.

2.3. Triple-objective optimization function

The triple-objective optimization model is formulated as follows:

(1) Minimize the average temperature factor (F), reflecting overall temperature uniformity:

$$F=\frac{\frac{1}{S}\int T-T_{\min}}{T_{\max}-T_{\min}} \tag{5}$$

(2) Minimize the fluid dissipation power (W_f), reflecting flow resistance loss:

$$W_f=\mu\int_\Gamma\nabla u\cdot\nabla u du\tau\Gamma+\int_\Gamma\alpha(\gamma)u\cdot ud\Gamma \tag{6}$$

(3) Minimizing the entry dissipation rate (W_h) reduces the thermal resistance analogously to electrical impedance minimization, directly enhancing the temperature uniformity [31,35–37].

The EDR quantifies irreversible losses in the heat transfer capability of the system, which is proportional to the square of the temperature gradient (∇T). Consequently, minimizing the EDR promotes reduced temperature gradients, improving temperature uniformity and global heat transfer efficiency.

$$W_h=\int\Omega\left(k(\gamma)/T^2\right)\cdot\left|\nabla T^2\right|d\Omega \tag{7}$$

The total objective function J was constructed as a normalized weighted sum:

$$J=\omega_T\frac{F}{F_0}+\omega_f\frac{W_f}{W_{f_0}}+\omega_g\frac{W_h}{W_{h_0}} \tag{8}$$

Weighting coefficients were derived from the Pareto-front analysis: $\omega_T=0.2$(for temperature),$\omega_f=0.2$(for flow resistance),$\omega_h=0.6$(for entransy dissipation rate), and $\omega_T+\omega_f+\omega_h=1$. The normalized reference values F_0, W_{f_0}, W_{h_0}were obtained from a simulation with a uniform material distribution.

2.4. Solution procedure and optimization results

The triple-objective optimization problem was solved using the MMA. Convergence was achieved when the relative change in design variables fell below 1×10^{-6}. The computational workflow for topology optimization is illustrated in Fig. 3. Four optimized configurations (M1–M4) were obtained. As shown in Fig. 4, M1 was established as the traditional benchmark model. A dual-objective optimization strategy was implemented to minimize the average temperature factor and fluid dissipation power, using a single-inlet single-outlet layout. M2 was designed as an innovative core configuration. The entransy dissipation rate was introduced as the third objective of the single-inlet single-outlet layout. Thus, a triple-objective optimization framework was constructed. M3 was developed using a dual-inlet dual-outlet layout. A dual-objective optimization was performed for this configuration. The effects of the inlet and outlet configurations were evaluated. M4 integrates the triple-objective optimization with a dual-inlet-dual-outlet layout. The synergistic mechanisms between the objective functions and the flow channel topology were comprehensively investigated. These optimized configurations were subsequently reconstructed as 3D models for thermofluidic performance analysis.

3. Numerical implementation and validation

3.1. 3D model reconstruction and parameter settings

The 2D topological configurations were extruded normal to the plane by 10 mm to obtain 3D solid models as shown in Fig. 5. All models had the same geometric parameters: channel height = 10 mm, channel width = 10 mm, substrate thickness = 4 mm as shown in Table 2, so that the comparative analysis was reasonable and fair. (See Table 3.)

3.2. Numerical method

The SST k-ω turbulence model was employed to accurately capture flow separation effects at low Reynolds numbers, accounting for complex flow behavior within microchannels. The validity of the turbulence model had been tested in slotted heat exchangers [38]. The computational domain adopted half-symmetric model as shown in Fig. 6. The inlet was set to a total mass flow rate of 2 kg/s, and the outlet was set to the pressure boundary condition. A constant heat flux of 300 W/cm^2 was imposed on the circular heat source area (radius of 5 cm). Adiabatic no-slip conditions were applied to all the other walls. The convergence requirement for the continuity and momentum equations was set at residuals $<10^{-6}$ and for the energy equation at residuals $<10^{-8}$.

Table 1
Physical parameters and optimization settings.

Parameter	Value	Material
Heat Source Power (W)	23,550	
Fluid Viscosity (Pa·s)	0.001	water
Fluid Density (kg/m^3)	1000	water
Fluid Thermal Conductivity [W/(m·K)]	0.6	water
Fluid Specific Heat [J/(kg·K)]	4200	water
Solid Density (kg/m^3)	8960	Copper
Solid Thermal Conductivity [W/(m·K)]	407	Copper
Solid Specific Heat [J/(kg·K)]	418	Copper
Inlet Temperature (K)	293.15	Copper
Projection Slope Parameter,β	16	
Projection Threshold,η	0.5	
Convergence Tolerance	1e-6	
Darcy Number, *Da*	1e4	

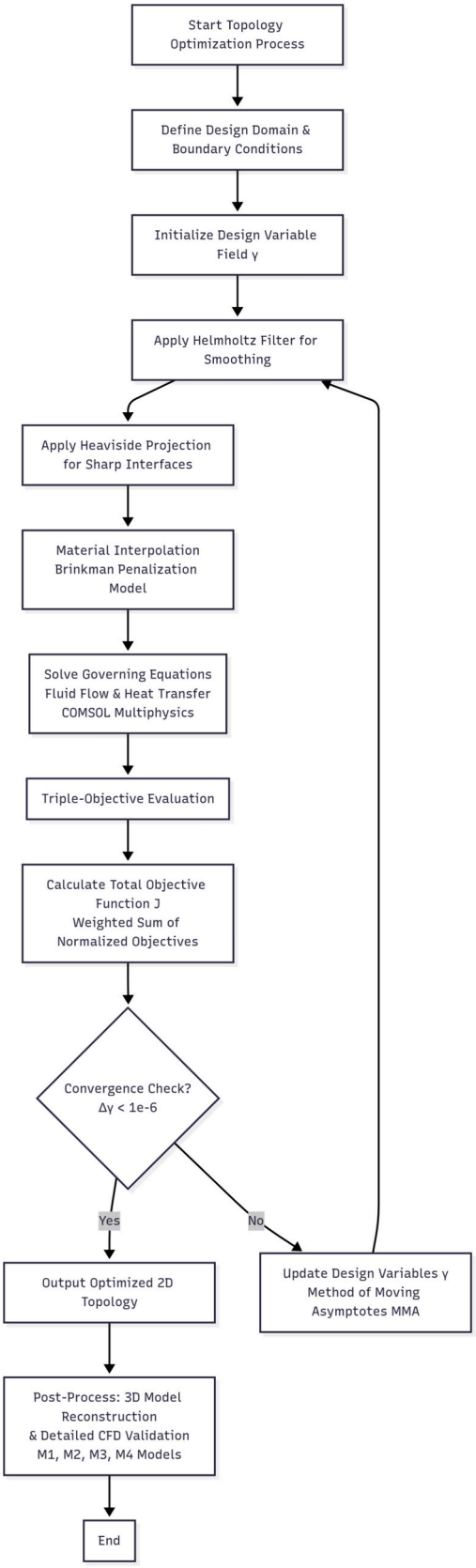

Fig. 3. Flowchart of the topology optimization procedure.

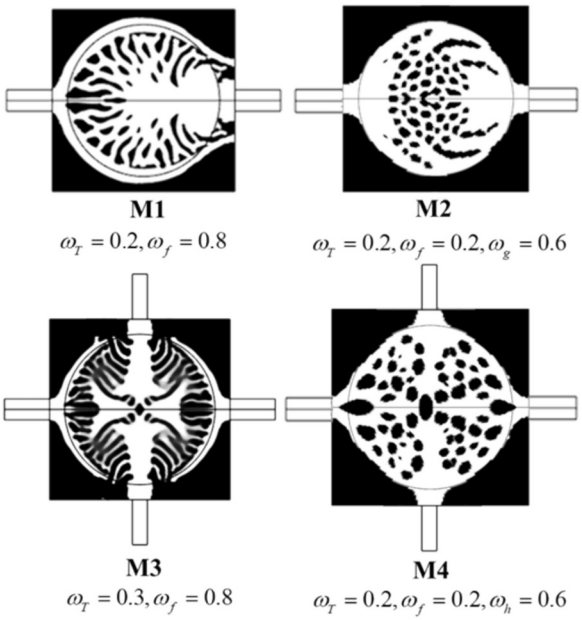

Fig. 4. Optimized configurations.
(M1: Dual-obj Single I/O; M2: Triple-obj Single I/O; M3: Dual-obj Dual I/O; M4: Triple-obj Dual I/O)

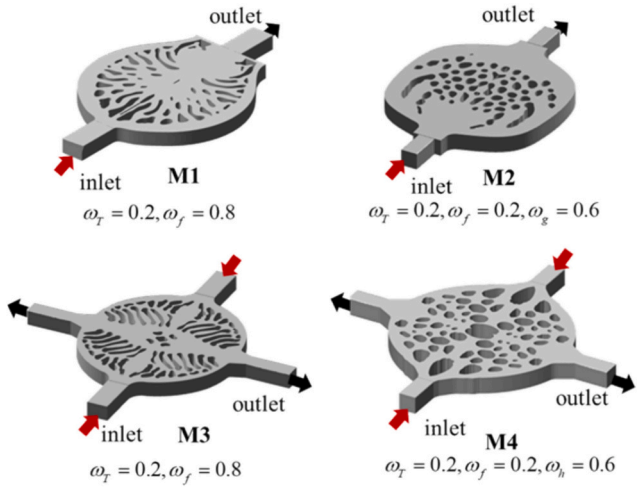

Fig. 5. Three-dimensional solid model of topology optimization configuration (M1-M4).

Table 2
Heat exchanger dimensions.

Parameter	Value (mm)
Overall height, H	14
Overall length, L	120
Overall width, W	120
Flow channel height,H_{ch}	10
Flow channel Inlet width,W_{ch}	10

3.3. Thermodynamic evaluation parameters

The heat transfer performance was evaluated by the Nusselt number (Nu) [39]:

$$Nu = \frac{q \cdot D_h}{k_f (T_w - T_f)} \tag{9}$$

Table 3
Comparison of Thermal Flow Performance of M1-M4.

Structure	T_{max} (K)	T_{avg}(K)	Pressure Drop (kPa)	F	PEC
M1	459.59	399.01	120.31	17.20	1.000
M2	423.11	376.74	294.07	17.16	1.007
M3	410.78	376.79	61.60	17.09	1.574
M4	407.79	379.41	46.70	17.13	1.678

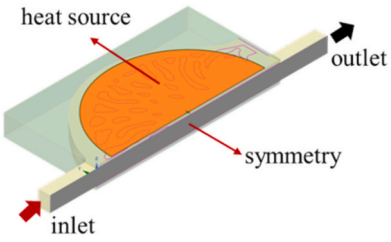

Fig. 6. Computational domain.

where q is the heat flux, T_w is the average heated-surface temperature, and T_f is the average bulk-fluid temperature.

The hydraulic diameter(D_h)is defined as:

$$D_h = 2\frac{W_{ch}H_{ch}}{(W_{ch}+H_{ch})} \tag{10}$$

Where W_{ch} and H_{ch} denote the width and height of the fluid channel, respectively.

The performance evaluation criterion (PEC) was used for a overall comparison of thermal-hydraulic performance.

$$PEC = \frac{(Nu_i/Nu_0)}{\sqrt[3]{\Delta P/\Delta P_0}} \tag{11}$$

where baseline model M1 was used as the reference.Nu_i and Δp_i represent the average Nusselt numbers and inlet-outlet pressure drops of the evaluated models (M2, M3, and M4), respectively.

3.4. Grid-Independence verification

In order to verify the grid-independence of model M1, the convergence of solution at 3,915,746 cells was tested. The average temperature of heated surface and inlet-outlet pressure drop changed less than 1 % as shown in Fig. 7. To achieve a balance between accuracy and efficiency, 4,267,935 elements were used in following simulations.

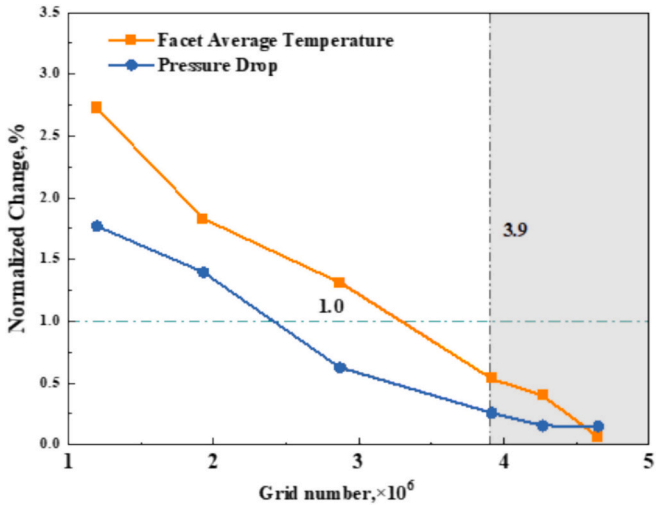

Fig. 7. Grid independence test for Model M1.

4. Analysis of numerical simulation results

4.1. Influence of objective function on topology

4.1.1. Flow characteristics comparative analysis

Fig. 8 showed the comparison of the velocity distributions in the central plane for M1 and M2. In Model M1, the low-velocity regions (0–4 m/s) were concentrated at the channel branch ends and corners, forming dead-flow zones. The high-velocity regions (12–20 m/s) were predominantly concentrated in the main outlet channel. The uneven velocity field indicated that the flow resistance was not uniformly distributed in the whole channel network. Thus, the coolant was not uniformly allocated in the heated area. A large decrease in the effective heat transfer area utilization was caused.

In order to further verify the above observation, the velocity profiles along the central axis were shown in Fig. 9.The above observation was further verified by the quantitative validation.M1 exhibited serious maldistribution of flow uniformity. Sharp velocity peaks occurred at x = 0.04 m and x = 0.12 m, corresponding to channel bifurcations. The flow separation dominated at the two positions. The velocity suddenly decreased at x = 0.16 m and then increased to 16–18 m/s near the outlet (x > 0.16 m). This confinement indicated that the main flow path concentrated, and the velocity in the branch section was lower than 8 m/s. The above observation was further verified by the quantitative validation.

In contrast, M2 exhibited obviously improved flow uniformity. The low-velocity zone (0–4 m/s) was greatly decreased. The medium-high velocity zone (8–16 m/s) expanded to the wider area. This spatial improvement was quantitatively validated in Fig. 9. The velocity along the central axis was larger than 8 m/s. No abrupt drops happed. The velocity transition from inlet to outlet was smooth and continuous. The extreme segregation shown in M1 was eliminated. This improvement mainly benefited from introducing entransy dissipation rate as the third objective. To reduce the EDR, lower temperature gradients are favored, which drives the TO algorithm to generate the flow channel that supports uniform coolant distribution. Inefficient low-velocity zones were effectively suppressed, and regions with excessively concentrated flow resistance and energy dissipation were mitigated. As a result, the more uniform distribution of flow resistance and rational coolant distribution were achieved.

4.1.2. Heat transfer characteristics comparative analysis

Temperature distributions on the heated surfaces of M1 and M2 were shown in Fig. 10. The temperature distribution on the heated surface of M1 was highly nonuniform (300–440 K). A close correspondence was observed between the spatial locations of the high-temperature hotspots (420–440 K) and the identified low-velocity flow regions. Severely insufficient heat dissipation in the hotspots was caused by the nonuniform coolant distribution. M2 exhibited a more uniform temperature field. This improvement was achieved by a more uniform flow distribution. Elimination of the extreme 440 K hotspot was accomplished. The area with temperatures exceeding 400 K was significantly reduced. The main temperature range was 340 K and 400 K. The minimization of entransy dissipation played a key role in this improvement. The dead-flow zones were eliminated using a driven topology structure. Local overheating was observed to be suppressed. The better match between the coolant flow distribution and spatial heat load was enforced. Consequently, the uniformity of the temperature field was significantly enhanced as a direct result. This uniformity is the key indicator for optimization.

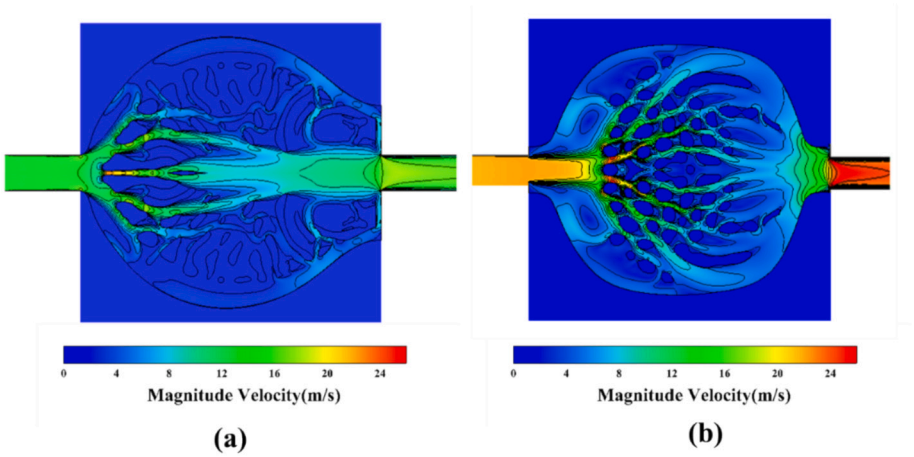

Fig. 8. Velocity Contour of (a) M1 and (b) M2.

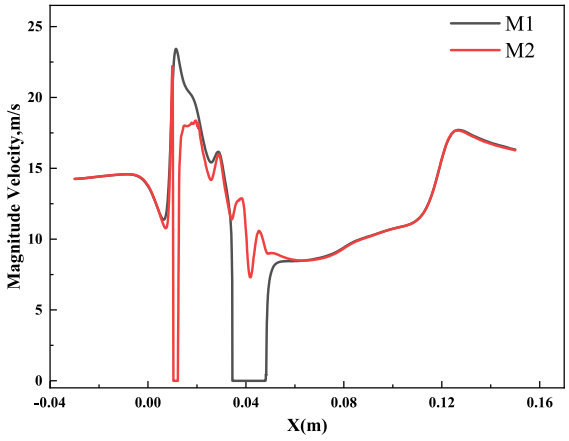

Fig. 9. Velocity profiles along central axis for M1 and M2.

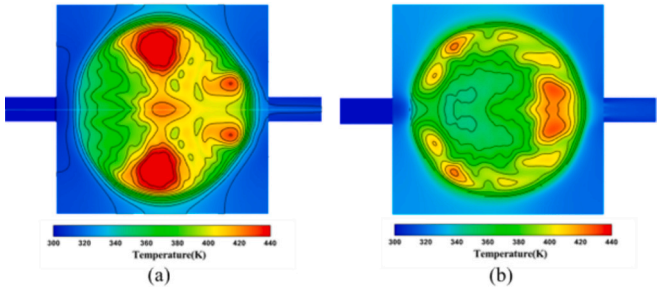

Fig. 10. Temperature Contour of (a) M1 and (b) M2.

4.2. *Influence of inlet/outlet configuration on topology*

4.2.1. *Flow characteristics comparative analysis*

The velocity distributions in central plane for M3 and M4 are shown in Fig. 11. The flow was significantly nonuniform (0–16 m/s) in M3, and low-velocity zones (0–5 m/s) were concentrated at the channel edges far from the inlets. It indicated flow separation and dead zones. High-velocity zones (10–16 m/s) appeared near direct path close to outlets. To quantitatively resolve these flow characteristics, Fig. 12 presented velocity profiles along the central axis. M3 exhibited pronounced velocity fluctuations. Sharp drops to $\leq$2 m/s occurred at positions x = −0.04 m and x = 0.04 m, corresponding to regions distant from inlets. Simultaneously, velocity peaks exceeding 10 m/s appeared near outlets

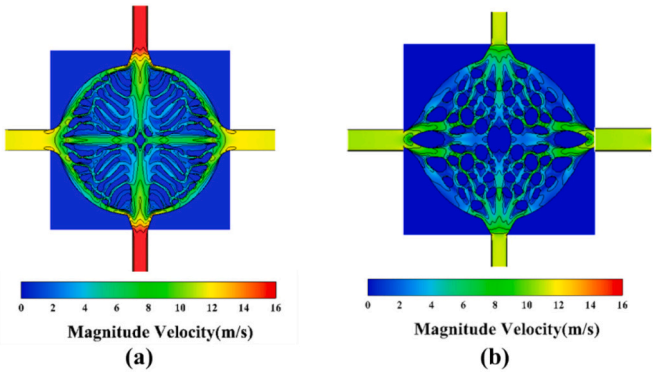

Fig. 11. Velocity Contour of (a) M3 and (a) M4.

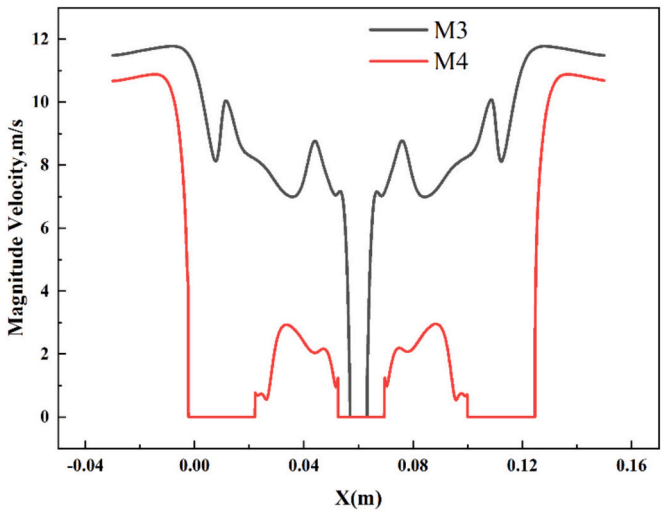

Fig. 12. Velocity profiles along central axis for M3 and M4.

(x > 0.08 m). Such maldistribution confirms the inefficient coolant allocation observed in Fig. 11.

In contrast, M4 totally restructured flow behavior. As shown in Fig. 11, almost no near deep blue stagnant zones (0–4 m/s) appeared, and the green/yellow zone (8–12 m/s) covered the whole heated surface uniformly. This spatial transformation is quantitatively validated in Fig. 12, M4 maintained velocities above 8 m/s along the entire central axis. There was no abrupt drop, and a smooth transition appeared

between inlets and outlets. A more balanced flow allocation was achieved between the two inlets. The above improvements were attributed to the EDR minimization objective. Under the dual-inlet and dual-outlet constraints, the minimization objective guided the topological reconstruction of the flow channels. Three key improvements were realized: the flow dead zones at the channel terminals were eliminated, concentrated jet effects at the inlets were suppressed, and a collaborative flow network was formed between the dual inlets. This network covers the heated surfaces and optimizes the flow resistance distribution. Effective coolant coverage over the entire heated area was achieved using a dual-inlet drive.

4.2.2. Heat transfer characteristics comparative analysis

The temperature distribution of heated-surface for M3 and M4 were shown in Fig. 13. The thermal management deficiencies were observed in M3. appeared between 300 and 322 K. The extreme temperature difference appeared between the two inlets, and reached 110 K. The dual-inlet configuration failed to realize the radial diffusion of coolant. The heat dissipation of high heat flux area was ineffective.

The uniformity of temperature was greatly improved at M4. The operational area was between 300 and 410 K. There were no hot spots appearing at over 410 K. T The high-temperature area at above 400 K reduced. The main temperature distribution was concentrated between 344 and 388 K. Local overheating and low-temperature redundancy were suppressed through the entransy dissipation mechanism. The precise alignment between the temperature distribution and spatial thermal load was achieved.

4.3. Comprehensive performance comparative analysis

M4 demonstrated a significant performance enhancement. The PEC value of 1.675 was attained based on M4, and the above value increased 67.5 % compared with M1, and then an improvement of 6.6 % over M3 was found. The decrease in the average temperature factor was 0.07 compared with M1. The triple-objective framework overcame the limitation of the conventional objective. Thermal management enhancement was focused on M2 (PEC = 1.026). In addition, M4 achieved three breakthroughs: the maximum temperature was decreased to 407.79 K, the pressure drop was stably controlled at 46.70 kPa, and the temperature uniformity was enhanced.

Significant differences in flow resistance characteristics were observed. The pressure increased to 294.07 kPa in M2 because of the complexity of the flow path. The improvement in M2 was 144 % compared with M1. It was suggested that a dual-inlet–dual-outlet configuration could effectively solve this problem.

The pressure was decreased to 46.7 kPa in M4. The pressure was decreased by 24.2 % compared with M3. The temperature uniformity was enhanced by adjusting the flow distribution efficiency with a two-outlet structure.

5. Conclusion

This study establishes a triple-objective TO framework that integrates the entransy dissipation rate (EDR) with the average temperature factor and fluid dissipation power. This framework was applied to the design of a microchannel system for BNCT lithium target. Key conclusions of the study are:

(1) Validation of EDR minimization: The triple-objective single-inlet/outlet model (M2) reduced the peak temperature by 20 % compared to the dual-objective model (M1), significantly improving temperature uniformity.
(2) Synergy of layout and objectives: The dual-inlet/outlet triple-objective model M4 maintained an average temperature level of M2 at 379.41 K, controlled peak temperature at 407.79 K, reduced pressure drop by 24.2 % relative to M3 to 46.7 kPa, and improved PEC by 67.5 % over M1.
(3) Multi-objective tradeoff balancing: The triple-objective framework could reconcile the conflicts between temperature uniformity, heat dissipation efficiency, and flow resistance. While M2 prioritized thermal management, M4 simultaneously achieved three key performance milestones: a 24.2 % reduction in pressure drop relative to M3, and reduced pressure drop to 46.7 kPa, a 20 % decrease in peak temperature compared to M1, down to 407.79 K, and significantly enhanced temperature uniformity.

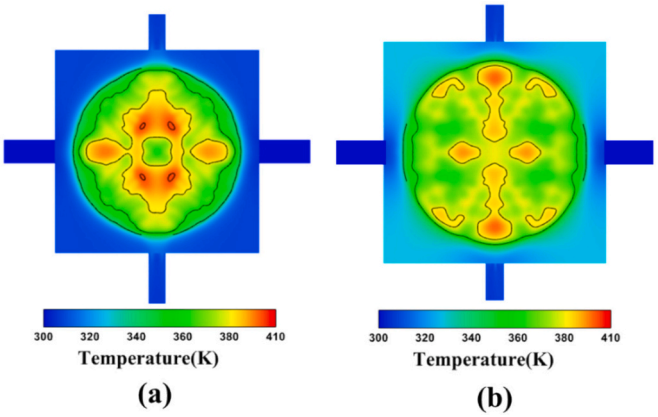

Fig. 13. Temperature Contour of (a) M3 and (b) M4.

An innovative design for BNCT lithium target heat exchangers was provided, and a new paradigm for an efficient microchannel heat sink design was proposed in this study.

CRediT authorship contribution statement

Zhao Xijun: Writing – original draft, Validation, Software, Methodology, Investigation, Funding acquisition, Data curation, Conceptualization. **Qin Kaiwen:** Writing – review & editing, Supervision, Resources, Project administration, Methodology, Funding acquisition, Data curation. **Lv Tingxiang:** Writing – review & editing, Resources, Methodology, Data curation. **Yang Si:** Project administration, Methodology, Investigation. **Zheng Wei:** Project administration, Funding acquisition. **Li Jun:** Resources, Data curation. **Tang Xiaobin:** Writing – review & editing, Validation, Supervision.

Declaration of competing interest

The authors declare that they have no known competing financial interests or personal relationships that could have appeared to influence the work reported in this paper.

Acknowledgements

This work was supported by Project supported by the National Natural Science Foundation of China (Grant No. 12575362), the Graduate Research Innovation Program Project of NUAA (Grant No. xcxjh20240611), the Graduate Research Innovation Program Project of Jiangsu Province (Grant No. KYCX24_0617).

Data availability

Data will be made available on request.

References

[1] S. Kawabata, M. Suzuki, K. Hirose, H. Tanaka, T. Kato, H. Goto, Y. Narita, S. Miyatake, Accelerator-based bnct for patients with recurrent glioblastoma: a multicenter phase ii study, Neuro Oncol. Adv. 3 (1) (2021) vdab067.

[2] D.M. Minsky, A.J. Kreiner, A.A. Valda, Ab-bnct beam shaping assembly based on 7li(p,n)7be reaction optimization, Appl. Radiat. Isot. 69 (12) (2011) 1668–1671.

[3] R. Inoue, F. Hiraga, Y. Kiyanagi, Optimum design of a moderator system based on dose calculation for an accelerator driven boron neutron capture therapy, Appl. Radiat. Isot. 88 (2014) 225–228.

[4] H. Kumada, A. Matsumura, H. Sakurai, T. Sakae, M. Yoshioka, H. Kobayashi, H. Matsumoto, Y. Kiyanagi, T. Shibata, H. Nakashima, Project for the development of the linac based nct facility in university of Tsukuba, Appl. Radiat. Isot. 88 (2014) 211–215.

[5] H. Tanaka, Y. Sakurai, M. Suzuki, S. Masunaga, T. Mitsumoto, K. Fujita, G. Kashino, Y. Kinashi, Y. Liu, M. Takada, K. Ono, A. Maruhashi, Experimental verification of beam characteristics for cyclotron-based epithermal neutron source (c-bens), Appl. Radiat. Isot. 69 (12) (2011) 1642–1645.

[6] S. Kamada, M. Takada, M. Suda, T. Hamano, H. Imaseki, M. Hoshi, R. Fujii, M. Nakamura, H. Sato, A. Higashimata, S. Arai, Development of target system for intense neutron source of p-li reaction, Appl. Radiat. Isot. 88 (2014) 195–197.

[7] Therapy, neutron target for boron, 2025.

[8] J. Li, G.P. Peterson, P. Cheng, Three-dimensional analysis of heat transfer in a micro-heat sink with single phase flow, Int. J. Heat Mass Transf. 47 (19–20) (2004) 4215–4231.

[9] S. Nakamura, H. Igaki, M. Ito, H. Okamoto, S. Nishioka, K. Iijima, H. Nakayama, M. Takemori, S. Imamichi, T. Kashihara, K. Takahashi, K. Inaba, K. Okuma, N. Murakami, Y. Abe, Y. Nakayama, M. Masutani, T. Nishio, J. Itami, Characterization of the relationship between neutron production and thermal load on a target material in an accelerator-based boron neutron capture therapy system employing a solid-state li target, PLoS One 14 (11) (2019) e0225587.

[10] D.A. Allen, T.D. Beynon, What is the best proton energy for accelerator-based bnct using the reaction? Med. Phys. 27 (5) (2000) 1113–1118.

[11] C. Willis, D. John Lenz, L.S. Llc Swenson, High-power lithium target for accelerator-based bnct, Proc. LINAC08 12 (2008) 223–225.

[12] D.A. Swenson, Compact, inexpensive, epithermal neutron source for bnct, AIP Conf. Proc. 475 (1) (1999).

[13] L. Porra, T. Seppälä, L. Wendland, H. Revitzer, H. Joensuu, P. Eide, H. Koivunoro, N. Smick, T. Smick, M. Tenhunen, Accelerator-based boron neutron capture therapy facility at the Helsinki university hospital, Acta Oncol. 61 (2) (2022) 269–273.

[14] B. Bayanov, V. Belov, V. Kindyuk, E. Oparin, S. Taskaev, Lithium neutron producing target for binp accelerator-based neutron source, Appl. Radiat. Isot. 61 (5) (2004) 817–821.

[15] S. Nakamura, H. Igaki, M. Ito, S. Imamichi, T. Kashihara, H. Okamoto, S. Nishioka, K. Iijima, T. Chiba, H. Nakayama, M. Takemori, Y. Abe, T. Kaneda, K. Takahashi, K. Inaba, K. Okuma, N. Murakami, Y. Nakayama, M. Masutani, T. Nishio, J. Itami, Neutron flux evaluation model provided in the accelerator-based boron neutron capture therapy system employing a solid-state lithium target, Sci. Rep. 11 (1) (2021) 8090.

[16] S. Zeng, B. Kanargi, P.S. Lee, Experimental and numerical investigation of a mini channel forced air heat sink designed by topology optimization, Int. J. Heat Mass Transf. 121 (2018) 663–679.

[17] G.H. Yoon, Topological design of heat dissipating structure with forced convective heat transfer, J. Mech. Sci. Technol. 24 (6) (2010) 1225–1233.

[18] H. Li, X. Ding, F. Meng, D. Jing, M. Xiong, Optimal design and thermal modelling for liquid-cooled heat sink based on multi-objective topology optimization: an experimental and numerical study, Int. J. Heat Mass Transf. 144 (2019) 118638.

[19] Y. Joo, I. Lee, S.J. Kim, Topology optimization of heat sinks in natural convection considering the effect of shape-dependent heat transfer coefficient, Int. J. Heat Mass Transf. 109 (2017) 123–133.

[20] J. Alexandersen, O. Sigmund, N. Aage, Large scale three-dimensional topology optimisation of heat sinks cooled by natural convection, Int. J. Heat Mass Transf. 100 (2016) 876–891.

[21] V. Subramaniam, T. Dbouk, J.L. Harion, Topology optimization of conductive heat transfer devices: an experimental investigation, Appl. Therm. Eng. 131 (2018) 390–411.

[22] X. Han, H. Liu, G. Xie, L. Sang, J. Zhou, Topology optimization for spider web heat sinks for electronic cooling, Appl. Therm. Eng. 195 (2021) 117154.

[23] B. Zhang, J. Zhu, G. Xiang, L. Gao, Design of nanofluid-cooled heat sink using topology optimization, Chin. J. Aeronaut. 34 (2) (2021) 301–317.

[24] F. Yanling, Y. Xiaoqing, Z. Tiantian, Micro-channel heat sink design based on multi-objective topology optimization method, Electronic Test 9 (2021) 45–47, 79.

[25] D. Adalja, K. Kalita, L. Epová, P. Patel, N. Mashru, P. Jangir Arpita, Advancing truss structure optimization—a multi-objective weighted average algorithm with enhanced convergence and diversity, Res. Eng. Des. 25 (2025) 104241.

[26] G. Srikanth, D. Nimma, R.V.S. Lalitha, P. Jangir, N.V.S. Kumari Arpita, Food security based marine life ecosystem for polar region conditioning: remote sensing analysis with machine learning model, Remote Sens. Earth Syst. Sci. 8 (1) (2025) 65–73.

[27] M. Aljaidi, N. Mashru, P. Patel, D. Adalja, P. Jangir, S.B. Arpita, M. Khishe Pandya, Morime: a multi-objective rime optimization framework for efficient truss design, Res. Eng. Des. 25 (2025) 103933.

[28] P. Jangir, S.P. Arpita, S.B. Agrawal, A. Pandya, S. Parmar, G.G. Kumar, L. Abualigah Tejani, A cooperative strategy-based differential evolution algorithm for robust pem fuel cell parameter estimation, Ionics 31 (1) (2025) 703–741.

[29] M.K.P.J. Abualigah, Innovative diversity metrics in hierarchical population-based differential evolution for pem fuel cell parameter optimization, Eng. Rep. 7 (1) (2025) e13065.

[30] M. Aljaidi, S.P. Agrawal, P. Jangir, S.B. Pandya, A. Parmar, A.F. Arpita, B. I. Alkoradees, M. Khishe Trivedi, A two stage differential evolution algorithm for parameter estimation of proton exchange membrane fuel cell, Sci. Rep. 15 (1) (2025) 5329–5354.

[31] X. Zaizhong, Augmentation and Optimization on Heat Conduction and Convection Processes, Doctor Tsinghua University, Beijing, 2001.

[32] F. Wang, B.S. Lazarov, O. Sigmund, On projection methods, convergence and robust formulations in topology optimization, Struct. Multidiscip. Optim. 43 (6) (2011) 767–784.

[33] J.K. Guest, J.H. Prévost, Topology optimization of creeping fluid flows using a darcy–stokes finite element, Int. J. Numer. Methods Eng. 66 (3) (2006) 461–484.

[34] Y. Lv, S. Liu, Topology optimization and heat dissipation performance analysis of a micro-channel heat sink, Meccanica 53 (15) (2018) 3693–3708.

[35] Q. Chen, X. Liang, Z. Guo, Entransy theory for the optimization of heat transfer – a review and update, Int. J. Heat Mass Transf. 63 (2013) 65–81.

[36] X. Chen, T. Zhao, M. Zhang, Q. Chen, Entropy and entransy in convective heat transfer optimization: a review and perspective, Int. J. Heat Mass Transf. 137 (2019) 1191–1220.

[37] C. Su, T. Zhao, Z. Guo, Generalized entransy dissipation and its application in heat conduction optimizations with arbitrary boundary conditions, Int. J. Heat Mass Transf. 216 (2023) 124534.

[38] D.F.W. Wróblewski, Heat transfer modelling in a rotating cavity using the sst k- ω turbulence model, Arch. Mech. 5 (66) (2014) 343–364.

[39] H.F. Al-Neama, Z. Khatir, N. Kapur, J. Summers, An experimental and numerical investigation of chevron fin structures in serpentine minichannel heat sinks, Int. J. Heat Mass Transf. (2018) 1213–1228.